The Astronomical Journal, 155:102 (9pp), 2018 February https://doi.org/10.3847/1538-3881/aaa422

In the Crosshair: Astrometric Exoplanet Detection with *WFIRST*'s Diffraction Spikes

Peter Melchior[1], David Spergel[1,2], and Arianna Lanz[1]
[1] Department of Astrophysical Sciences, Princeton University, Peyton Hall, Princeton, NJ 08544, USA; peter.melchior@princeton.edu
[2] Center for Computational Astrophysics, Flatiron Institute, 162 5th Avenue, NY 10010, USA
Received 2017 August 11; revised 2017 November 19; accepted 2017 December 17; published 2018 February 1

Abstract

WFIRST will conduct a coronagraphic program that characterizes the atmospheres of planets around bright nearby stars. When observed with the *WFIRST* Wide Field Camera, these stars will saturate the detector and produce very strong diffraction spikes. In this paper, we forecast the astrometric precision that *WFIRST* can achieve by centering on the diffraction spikes of highly saturated stars. This measurement principle is strongly facilitated by the *WFIRST* H4RG detectors, which confine excess charges within the potential well of saturated pixels. By adopting a simplified analytical model of the diffraction spike caused by a single support strut obscuring the telescope aperture, integrated over the *WFIRST* pixel size, we predict the performance of this approach with the Fisher-matrix formalism. We discuss the validity of the model and find that 10 μas astrometric precision is achievable with a single 100 s exposure of an $R_{AB} = 6$ or a $J_{AB} = 5$ star. We discuss observational limitations from the optical distortion correction and pixel-level artifacts, which need to be calibrated at the level of 10–20 μas so as to not dominate the error budget. To suppress those systematics, we suggest a series of short exposures, dithered by at least several hundred pixels, to reach an effective per-visit astrometric precision better than 10 μas. If this can be achieved, a dedicated *WFIRST* GO program will be able to detect Earth-mass exoplanets with orbital periods of $\gtrsim$1 year around stars within a few pc as well as Neptune-like planets with shorter periods or around more massive or distant stars. Such a program will also enable mass measurements of many anticipated direct-imaging exoplanet targets of the *WFIRST* coronagraph and a "starshade" occulter.

Key words: astrometry – methods: observational – planetary systems

1. Introduction

The *WFIRST* mission will use a repurposed 2.4 m telescope to conduct a program of studying dark energy, detecting planets through microlensing, imaging planets with a coronagraph, and using its wide field camera for general astrophysics (Spergel et al. 2013, 2015). As one of the primary science drivers for *WFIRST* is making precision measurements of weak gravitational lensing to characterize the nature of dark energy, *WFIRST* is being designed to have a very stable point spread function (PSF). *WFIRST* is operating at the thermally and dynamically stable L2 point and its thermal/mechanical design is optimized to minimize variations in the PSF. *WFIRST* has a wide field camera whose 18 Mercury Cadmium Telluride (HgCdTe) H4RG chips enable a 0.28 square degree field. The combination of this large field of view, which will image hundreds of bright *Gaia* (Gaia Collaboration et al. 2016) stars with each observation, and the stable PSF makes *WFIRST* a powerful instrument for astrometry.

WFIRST should be able to conduct a rich and diverse program that uses astrometry to address science questions ranging from the nature of dark matter, to testing stellar models, to searching for exosolar planets. The *WFIRST* science team reports (Spergel et al. 2013, 2015) describe some of these potential applications enabled by *WFIRST*'s ability to obtain submilli-arcsecond astrometry, even for stars as faint as 25th magnitude. Gould et al. (2015, hereafter G15) discuss *WFIRST* astrometry as part of the bulge survey. In this paper, we will focus on the capabilities of *WFIRST* bright star astrometry and its application to detecting exoplanets around nearby stars. *WFIRST*'s H4RG HgCdTe detectors are well suited for bright star astrometry because these CMOS detectors trap charges in pixels, unlike CCDs, which bleed.

In this work, we seek to understand how precisely one can determine stellar centroids of very bright stars given the design of *WFIRST*, foremost its PSF shape and pixel size. A similar investigation has been performed by G15. We extend that work in three main aspects: (1) G15 consider only imaging obtained as part of the *WFIRST* microlensing program, which has a fixed exposure time and dither pattern, and only uses the *H*-band. We investigate all available filters in the latest *WFIRST* design and a range of exposure times. (2) Because of the pixel-level artifacts, we specifically want to avoid a strong reliance of the centroid measurement on a small number of pixels, spreading out the signal over a larger area and rejecting the inner regions of the PSF even if they are not saturated. Our results are therefore more conservative than those of G15, who found that a sizable fraction of the statistical power stems from mildly saturated pixels in the core. (3) We attempt to determine the amount of uncorrected systematics and propagate these uncertainties to the final precision. By splitting a visit into several exposures, we explore the trade-offs between exposure time and systematics mitigation to achieve optimal per-visit astrometric precision.

Because we intentionally avoid the core regions, we can restrict our model to capture only the features that are relevant at high flux levels, namely the diffraction spikes, and we generate an analytic model that can be evaluated in all bands (Section 2). We estimate the sensitivity of that model to shifts in the centroid of the star with the Fisher-matrix approach in Section 3. In Section 4, we discuss how various observational effects limit the centroiding precision, and in Section 5, we investigate if *WFIRST* could successfully detect exoplanets

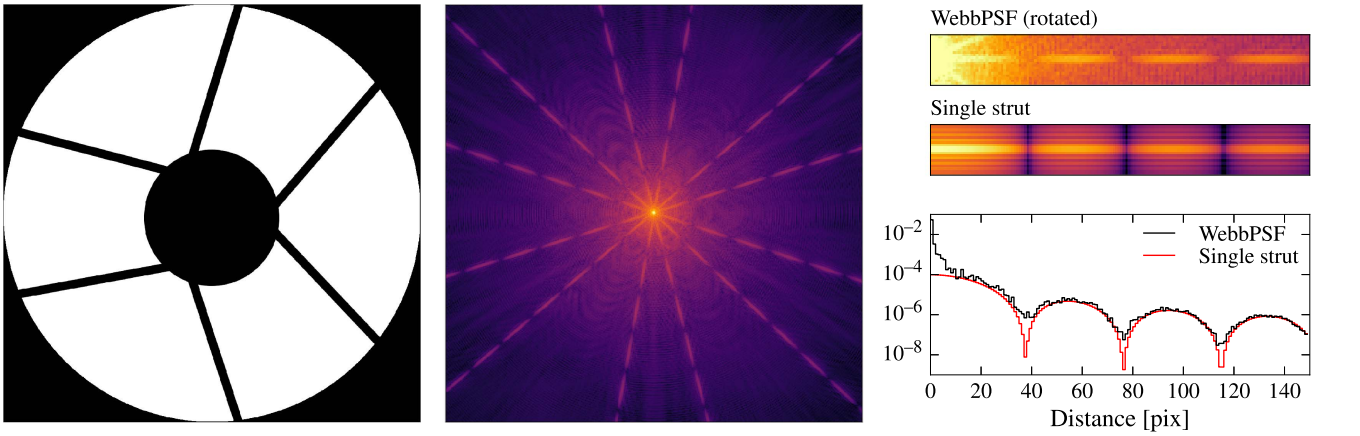

Figure 1. Left panel: *WFIRST* WFC Cycle 5 pupil for filters from R062 to H158. For reference, the aperture diameter is 2.37 m. Center panel: WebbPSF model of a monochromatic point source with $\lambda = 1$ μm in the center of the focal plane. Colors have logarithmic stretch. The presence of 12 diffraction spikes instead of 6 is a consequence of the non-radial alignment of the support struts. Right panel: visual comparison and horizontal profiles at peak intensity of the WebbPSF model and the analytical model of a single support strut given in Equation (5). The WebbPSF model was internally oversampled by a factor 10, rotated, and then downsampled to the final resolution.

from diffraction-spike measurements. We present our conclusions in Section 6.

Throughout this work, all magnitudes are in the AB system unless otherwise noted.

2. The PSF Model

We will approximate the shape of the PSF along a diffraction spike as being purely caused by a single support strut of the secondary mirror obscuring a part of the telescope aperture. In addition, we assume that the strut is rectangular with sidelengths a and b, pointing in a radial direction from the center to the edge of the pupil. The actual *WFIRST* pupil deviates from those assumptions: there is an inner and outer aperture radius, and the struts are not exactly radially aligned (see left panel of Figure 1).[3] We will nonetheless adopt this simplified pupil and investigate the accuracy of the model later.

In the Fraunhofer regime of geometrical optics, we can describe the electrical field $E(x, y)$ at the focal plane in angular coordinates as the Fourier transform of the rectangular obstruction:

$$E(x, y) = \mathrm{sinc}\left(\frac{\pi a \sin(x)}{\lambda}\right)\mathrm{sinc}\left(\frac{\pi b \sin(y)}{\lambda}\right). \quad (1)$$

The PSF intensity is given by the square of the electric field,

$$I(x, y) = \mathrm{sinc}^2(k_x x)\mathrm{sinc}^2(k_y y), \quad (2)$$

where we employed the small-angle approximation and introduced $k_x \equiv \pi a/\lambda$ and $k_y \equiv \pi b/\lambda$. This well-known result is not directly applicable, because the diffraction features are narrow compared to the pixel grid. We therefore need to account for the pixelation, i.e., each *WFIRST* pixel has a finite size $w = 0.11$ as, which amounts to an integration over the box-shaped pixel area

$$I_p(x, y) = \int dx' dy' I(x', y') \,\mathrm{rect}\left(\frac{x - x'}{w}\right)\mathrm{rect}\left(\frac{y - y'}{w}\right) \quad (3)$$

followed by sampling that function at the centers of a pixel grid enumerated with indices (i, j),

$$I_p(i, j) = I_p(x_i, y_j), \quad (4)$$

where $x_i = \left(i + \frac{1}{2}\right)w$. Given the form of Equation (3), the resulting function must be separable,

$$I_p(x, y \mid k_x, k_y, w) = I_p(x \mid k_x, w) I_p(y \mid k_y, w). \quad (5)$$

The analytical form of the one-dimensional $I_p(x)$ is given in Equation (21). A comparison between this PSF model of a single support strut and the WebbPSF[4] model (Perrin et al. 2012, 2014) of the entire pupil is show in right panel of Figure 1.

We can see that the analytical model correctly captures the main features of the diffraction spike, in particular, the location of the minima in the x-direction, from which we determine $a = 4.85$ cm. The profile in the y-direction, which contains almost all of the information about the stellar centroid, is shown in Figure 2, from which we infer $b = 84$ cm. Both values of a and b are in good agreement with measurements from the pupil image shown in the left panel of Figure 1.

It is worthwhile noting that the oscillations of the diffractions spikes are resolved with the *WFIRST* pixel scale w, even at $\lambda < 1$ μm, while the core of the PSF is undersampled. This is a consequence of the smaller length b of the support strut compared to the full aperture diameter.

On the other hand, we can also see the limitations of the analytical model: (1) It drastically underestimates the intensity in the center. We will therefore restrict the fitting range to outside of the first minimum in x-direction, i.e., $|x| > \lambda/a$, which corresponds to 39 pix at $\lambda = 1$ μm. (2) There is a floor of diffracted light from the centrally obscured pupil (see central panel of Figure 1), which reduces the dynamic range in the actual diffraction spike, especially in y-direction. At fixed x, it

[3] For observations well above 1 μm, an additional pupil mask is mounted directly on the filter, increasing the obscured areas of the pupil and noticeably changing the PSF and diffraction spike shapes, rendering our model inapplicable. Given the currently planned telescope operating temperature of 260 K, the pupil mask would only be used for the filters redward of H158, which we will therefore neglect in this study.

[4] http://www.stsci.edu/wfirst/software/webbpsf

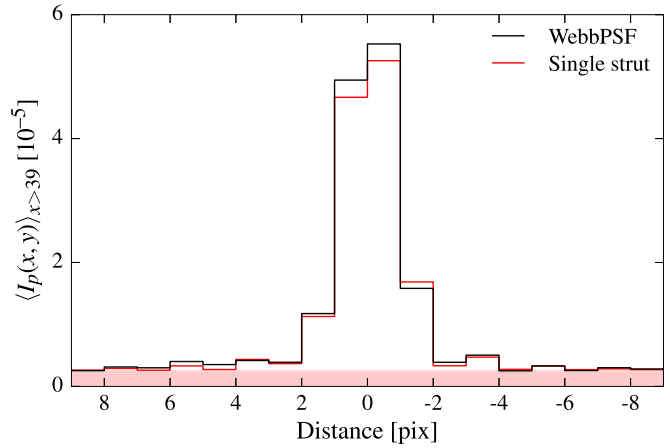

Figure 2. Comparison of the vertical profile of the diffraction spikes as predicted by WebbPSF and the analytical model of a single support strut given in Equation (5) for a point source with $\lambda = 1$ μm in the center of the focal plane. The area within the first diffraction minimum (here $x < 39$ pix) was excluded. The model underestimates the amount of diffracted light from the centrally obscured pupil, which can be approximated by a constant in y-direction with an amplitude of 0.2×10^{-5} (shown in *light red*).

Table 1
Thermal and Sky Background Intensities in the *WFIRST* Filter Bands, with a Spacecraft Operating Temperature of 260 K and Filter Throughputs Set to 0.95

Filter	$I_{\rm sky}$ [e$^-$ s^{-1} pix^{-1}]	$I_{\rm thermal}$ [e$^-$ s^{-1} pix^{-1}]
R062	0.638	0.023
Z087	0.464	0.023
Y106	0.453	0.023
J126	0.442	0.023
H158	0.437	0.052

Note. The filter names denote the central wavelength, e.g., Y106 implies $\lambda_c = 1.06$ μm.

can be approximated by a constant, but it reduces the contrast of the higher-order diffraction features. We will therefore restrict the fitting range to the inner three maxima, i.e., $|y| < 3\lambda/b$, or 6 pix at $\lambda = 1$ μm.

3. Centering on the Diffraction Spikes

We make use of the Fisher information to determine the precision with which we can fit for the centroid given the pattern of the diffraction spike in data D,

$$F_{i,j} = -\frac{\partial^2}{\partial\theta_i\,\partial\theta_j} \ln \mathcal{L}(D;\,\theta), \tag{6}$$

with two fit parameters $\theta = (x, y)$. We assume Gaussian and uncorrelated noise,[5] which leads to the familiar χ^2 form

$$\ln \mathcal{L} = -\frac{1}{2} \sum_{i,j\in\mathcal{V}} \frac{[D_{i,j} - Nf_{\rm strut} I_p(x_i - x,\, y_j - y)]^2}{\sigma_{i,j}^2}, \tag{7}$$

where the normalization accounts for the total flux that is incident on the strut: N is the total number of photons to reach the unobscured telescope aperture, and $f_{\rm strut} = ab/[(1-o)(d/2)^2\pi]$ is the fraction of the aperture covered by the strut. According to the WFIRST Cycle 6 telescope parameters, the mirror diameter $d = 2.37$ m, and the central obscuration o corresponds to 13.9%, resulting in $f_{\rm strut} \approx 0.01$.

The likelihood should only be evaluated for valid pixels $(i, j) \in \mathcal{V}$, which combines two conditions: the range in which the PSF model is a fair description of the actual diffraction spike (see Section 2), and an intensity limit set by the saturation level of the H4RG detectors, estimated at $I_p(i, j) < 1.2 \cdot 10^5$ e$^-$ (B. Rauscher 2017, private communication) with a gain of 2.

Because of the separability of I_p, we can express the elements of the Fisher matrix as

$$\begin{aligned}
F_{11} &= N^2 f_{\rm strut}^2 \sum_{i,j\in\mathcal{V}} \frac{I_p(y_j - y)^2}{\sigma_{i,j}^2} \left[\frac{\partial I_p(x_i - x)}{\partial x}\right]^2 \\
F_{22} &= N^2 f_{\rm strut}^2 \sum_{i,j\in\mathcal{V}} \frac{I_p(x_i - x)^2}{\sigma_{i,j}^2} \left[\frac{\partial I_p(y_j - y)}{\partial y}\right]^2 \\
F_{12} &= N^2 f_{\rm strut}^2 \sum_{i,j\in\mathcal{V}} \frac{I_p(x_i - x, y_j - y)}{\sigma_{i,j}^2} \frac{\partial I_p(x_i - x)}{\partial x} \frac{\partial I_p(y_j - y)}{\partial y}.
\end{aligned} \tag{8}$$

The one-dimensional derivatives are listed in Equation (22).

The final ingredient for the likelihood is the pixel noise variances, for which we assume a combination of Poisson, sky background, thermal emission, read-out noise, and dark current

$$\sigma_{i,j}^2 = Nf_{\rm strut} I_p(i, j) + I_{\rm sky} + I_{\rm thermal} + \sigma_{\rm ron}^2 + \sigma_{\rm dark}^2. \tag{9}$$

The read-out noise and dark currents are not yet known ($\sigma_{\rm ron} < 20$ e$^-$ pix^{-1} as per *WFIRST* Science Requirements). We adopt $\sigma_{\rm ron} = 5$ e$^-$ pix^{-1} and $\sigma_{\rm dark} = 0.015$ e$^-$ s^{-1} pix^{-1}. Thermal and sky background intensities, taken from the *WFIRST* exposure time calculator,[6] for different wavelengths are listed in Table 1.

The relevant quantity in this configuration is the uncertainty in the narrow y-direction,

$$\Delta_y^2 = [F^{-1}]_{22}, \tag{10}$$

where we marginalized over the uncertainty in the x-direction. However, *WFIRST* has $k = 6$ support struts at different angles ϕ_k, separated by approximately 30°, so that each of them can be used as an independent measurement of y with precision $\Delta_y \cos(\phi_k)$, resulting in a joint astrometric precision of either x or y of

$$\Delta_{\rm pos} \approx \sqrt{\frac{2}{6}[F^{-1}]_{22}}. \tag{11}$$

Note that a more precise measurement could be made by exploiting the fact that each diffraction spike carries information on x *and* y, modulated by ϕ_k, but the improvement is only of order $a/b \approx 5\%$ compared to Equation (11).

In Figure 3, we show the predicted precision for a $t = 100$ s exposure as a function of stellar magnitude. The model is calculated for a monochromatic star with a wavelength centered on the *WFIRST* filters, and the conversion between photon count and magnitude incorporates Cycle 6 specifications of the

[5] Correlated noise, e.g., from remapping the images onto an undistorted frame, can be considered by introducing a pixel covariance matrix in the following equations. We neglect it in this work because we expect correlated noise to not significantly alter our findings.

[6] https://wfirst.ipac.caltech.edu/sims/tools/wfDepc/wfDepc.html

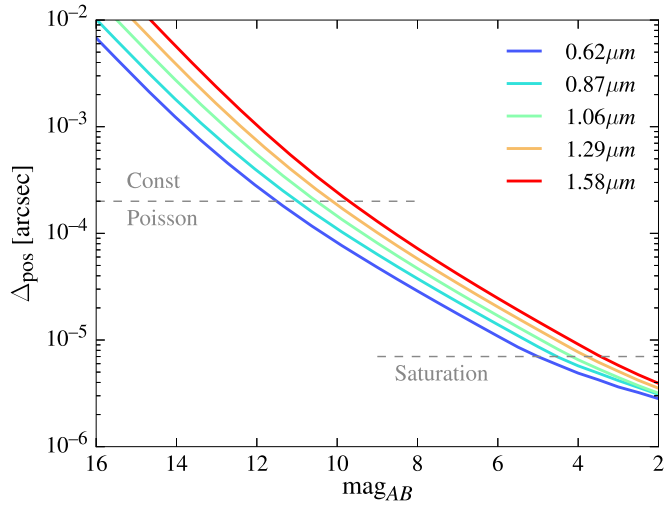

Figure 3. Astrometric precision as a function of stellar magnitude at the given wavelength for an exposure time of 100 s. The precision was averaged over 30 randomly chosen subpixel positions of the stellar center. The approximate locations for transitions between regimes that determine the shape of each curve are shown as horizontal dashed lines. The best precisions are achieved for the shortest wavelengths because the diffraction spike is narrowest.

optical transmission, detector efficiency, and contamination losses.

For fixed wavelength, the shape of the curve is dominated, from left to right: (1) by the constant, i.e., source-independent noise terms, foremost the sky background; (2) by the Poisson noise of the diffraction spike itself, scaling with $N^{-\frac{1}{2}}$; (3) by saturation, which impedes further improvements once the pixels in the region with a valid PSF model start to saturate, removing them from $\mathcal{V}$. We can see that for most of the magnitude range, the shortest wavelength yields the best astrometric precision because the diffraction spike is narrowest and sky and thermal emissions are lowest (cf. Table 1). But at short wavelengths, the steep profiles of the diffraction spikes saturate more quickly, even outside of the first diffraction minimum.

We conclude that the centering on the diffraction spikes of *WFIRST* allows for an astrometric precision of 10 μas (equivalent to $\approx 10^{-4}$ of a pixel) for a $R = 6$ star in a 100 s exposure. Our estimates in Figure 3 agree well with Gould et al. (2015), who find $\Delta_{\rm pos} \approx 10$ μas for a $H_{\rm Vega} = 3$ (approximately $H = 4.4$) star in a 52 s exposure, for which they utilized both the diffraction spikes and mildly saturated pixels. We want to stress that this combination is useful because mildly saturated pixels, which become saturated only after the first non-destructive read(s) of an exposure, provide a noticeable amount of astrometric information. The gain comes from utilizing pixels *between* the diffraction spikes, which requires an accurate PSF model for all pixels in question. Our simplified analytical model does not consider these areas and still captures the main aspects of the astrometric measurement in the highly saturated regime.

4. Limitations

So far we have calculated the astrometric precision one could achieve if the location of each pixel on the sky were perfectly known and reproducible, particularly important for long-running campaigns to establish variations in the stellar locations. Several effects will limit the precision in practice.

4.1. Optical Distortion Correction

As all optical instruments, *WFIRST* will exhibit geometric distortions that need to be corrected when image positions are mapped to locations on the sky. The precision of this mapping depends on the availability of an ideally distortion-free reference catalog, for instance from *Gaia*, or the ability to self-calibrate the distortions by constructing an internal master catalog of celestial object positions (e.g., Anderson & King 2003). We expect the self-calibration approach to yield superior results because *WFIRST* would be able to utilize stars (and possibly galaxies) below the magnitude limit of *Gaia* and would not have to extrapolate the apparent motions from the *Gaia* reference frame to the epoch of observations years later. Instead, one is either restricted to an instantaneous astrometric frame or needs to determine parallaxes and peculiar motions of suitable stars from repeated observations separated by years.

The approach has been employed with *HST* (Anderson & King 2003; Bellini et al. 2011) and ground-based imagers (Libralato et al. 2014), with astrometric precisions after correction of the order of 0.1–1 mas. This is at least an order of magnitude larger than what we seek to achieve for exoplanet detection, but the design and observation strategy of *WFIRST* should enable higher precision because of the thermally stable environment in L2 orbit and the abundance of calibration products from the microlensing survey. A detailed assessment of the optical distortion correction will be presented by Sanderson et al. (2017). Here, we adopt the following, admittedly optimistic, assumptions: a template library of optical distortion patterns and an accurate PSF model for each exposure, approximately 10000 unsaturated stars and compact galaxies per exposure, and 10 back-to-back exposures of approximately 100 s integration time, dithered by hundreds of pixels to uniquely determine the distortion template, should yield an astrometric precision in the central regions of each SCA of 10 μas.

4.2. Pixel-level Effects

In addition to residuals of the distortion correction, each pixel will be slightly offset from its assumed location in the focal plane. Several known detector effects are responsible for such shifts.

The sensitivity of the pixels is not strictly uniform. Barron et al. (2007) and Hardy et al. (2014) demonstrated that HgCdTe detectors exhibit subpixel quantum efficiency (QE) variations of several percent in some pixels. While *WFIRST* will be equipped with more advanced H4RG detectors, spatial offsets of a few percent of the pixel width need to be expected (M. Shao 2017, private communication). If the subpixel QE variations are uncorrelated between neighboring pixels, the per-pixel offset will be averaged over all pixels in Equation (7), but most damage would be done in those pixels with a high photon count. Considering Figures 1 and 2, most of the flux is accumulated in a narrow strip of approximately 4×120 pix, of which the inner 4×40 pix are masked. Over all 12 half-spikes, that amounts to 3840 pix. An uncorrected spatial offset of 1%w would then be averaged down to 18 μas, which demonstrates the benefit of spreading out the signal along the diffraction spikes. However, for stars with $R < 7$ or $H < 5$, subpixel QE variation would dominate the error budget. We anticipate that those variations can be calibrated with laboratory tests on the

ground and in flight by the *WFIRST* microlensing survey (Spergel et al. 2015, their Section 2.5.7) so that they will not limit the measurements proposed here.

Another relevant effect is nonlinearity, especially the so-called "brighter-fatter" effect, which presents itself as an increase in the width of point-sources as a function of source flux. It can be interpreted as the shrinking of the pixel depletion region due to the charges that accumulate during integration (Plazas et al. 2017, and references therein). As the total number of charges is expected to be conserved, the proposed solutions entail a re-apportioning of the pixels fluxes based on the brightness of the source across neighboring pixels. We expect that such a correction will be sufficient for our purposes. As long as the exposure times are fixed, any remaining residual of the correction would result in a very subtle additional blur that affects all exposures equally and does therefore not lead to additional astrometric residuals. It may, however, cause a mild degradation of the pixel-to-pixel contrast in the narrow direction and thus reduce the statistical power of the measurement.

Finally, we address persistence, which denotes a slowly fading imprint of bright objects after an exposure has been read out or even after the telescope has been moved. Should any preceding exposure induce persistence in a localized region, then the astrometry inferred from areas with a strong flux gradient in the responsible exposure will be biased. However, the affected regions are entirely predictable, and we can thus slew the telescope to avoid them, or mask them afterwards.

4.3. Additional Effects

During the exposures, the telescope may experience jitter and roll angle changes. Jitter is the solid-body motion caused predominantly by structural resonances induced by the reaction wheels of the attitude control system. It is likely that the occurrence of jitter can be diagnosed from telemetry data of that system, but even then its frequency, on the order of 10 Hz, will lead to an additional blurring of the entire exposure with a constant direction and an amplitude of up to 14 mas (Spergel et al. 2015). As the diffraction spikes are measured contemporaneously with the field stars, the blurring will reduce the centering sensitivity in the jitter direction but not induce an astrometric shift of the target star with respect to the stars that determine the astrometric solution. This remains true as long as the telescope responds as a solid body; if additional movements like "beam walk" are excited, they will have to be diagnosed and corrected from the optical distortion patters they create.

Rotations of the spacecraft, specifically roll angle changes, can be diagnosed from the location of stars in subsequent up-the-ramp samples of the exposure. Instantaneous roll angle changes (Riess et al. 2014, their Section 2.4.6) may require additional telemetry data for a reliable determination of the time-averaged roll angle during the exposure. A model of the PSF model should then be generated for each of the up-the-ramp samples to reflect the corresponding roll angles.

Finally, in our calculations we have assumed the point source to be monochromatic, while real stars have a continuous spectrum. This does not affect our findings. We anticipate that the wavelength dependence of the PSF will be well characterized as part of the *WFIRST* High-Latitude Survey weak-lensing program, and that the spectrum of most stars that are sufficiently bright to serve as targets will be known, so that we can calculate the PSF model for each such star.

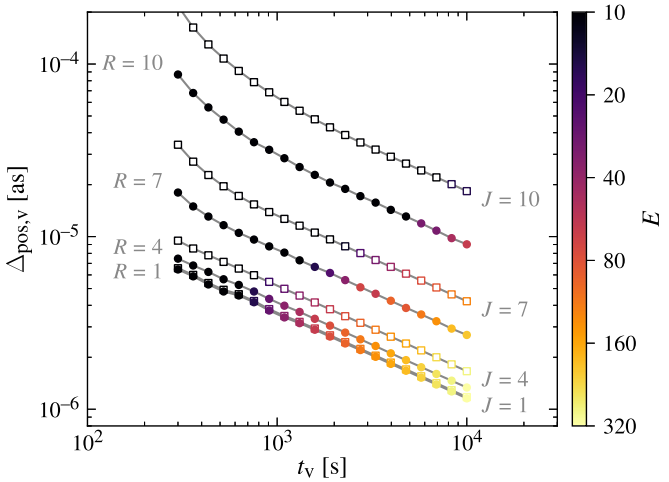

Figure 4. Per-visit astrometric precision as a function of integration time per visit $t_{\rm v}$ for $\lambda = 0.62\ \mu$m (R, *full circles*) and $\lambda = 1.06\ \mu$m (J, *open squares*). Shown are the best achievable precisions after optimizing over the number of exposures E, indicated by the color of the marker. Different lines correspond to the indicated stellar magnitude in the respective bands. Faint stars mandate few but long exposures to suppress Poisson noise; for bright stars, a large number of exposures is preferable to suppress systematic errors.

5. Exoplanet Detection with *WFIRST*

5.1. Per-visit Astrometry

Given the limitations we discussed in Section 4, it appears most beneficial to split a single visit of a target star into E exposures with integration times $t_{\rm e}$ chosen such that the astrometric precision from Section 3 is comparable to the systematics errors. If those errors are uncorrelated, the overall positional error is

$$\Delta_{\rm pos,v} = \frac{1}{\sqrt{E}}\sqrt{\Delta^2_{\rm pos}(t_{\rm e} \mid {\rm mag},\, \lambda) + \Delta^2_{\rm sys}}\,, \tag{12}$$

where $\Delta^2_{\rm pos}$ is given by Equation (11). We adopt a fiducial value $\Delta_{\rm sys} = 20\ \mu$as, noting that is could be different by up to a factor of several. To avoid spatial correlations of pixel-level artifacts and to aid the optical distortion correction, we need to slew the telescope between exposures by $\gtrsim$200 pix, which incurs a slew-and-settle time $t_{\rm ss} \approx 20$ s (J. Kruk 2017, private communication), resulting in a total visit time

$$t_{\rm v} = E\ t_{\rm e} + (E - 1)t_{\rm ss}. \tag{13}$$

Fixing $t_{\rm v}$ and varying E determines the best per-visit error of the program. For a reliable optical distortion correction, we assume that $E \geqslant 10$ and $t_{\rm e} \geqslant 10$ s.

The results are shown in Figure 4 for two central wavelengths and a range of stellar brightnesses and visit times, starting at the minimum of 280 s permitted under those constrains. Several aspects are remarkable. (1) As we have seen in Section 3, the astrometric precision at the same apparent brightness is better in R than in J. (2) For stars brighter than $R \approx 7$ or $J \approx 7$, the scaling is entirely dependent on the systematic error term in Equation (12), which is minimized by increasing the number of exposures E, even though a large fraction of the visit time is spent slewing. (3) For stars brighter than $R \approx 4$ or $J \approx 4$, the magnitude-dependent error term becomes irrelevant and there are thus no substantial gains in astrometric precision. (4) Positional uncertainties of

$\Delta_{\mathrm{pos,v}} \lesssim 10\ \mu$as can be achieved for $R < 7.5$ or $J < 6.5$ stars with visit times below 1000 s.

Besides the assumption of $\Delta_{\mathrm{sys}} = 20\ \mu$as, which sets the overall systematics floor, at which only increasing E provides any gains in accuracy, two other aspects of this forecast are worth pointing out. The minimum exposure time $t_{\mathrm{e}} \geqslant 10$ s is rather short for obtaining a sufficiently reliable optical distortion correction, which depends on precise measurements of reference stars. If it needs to be increased, the number of exposures E at a fixed visit time would have to be reduced accordingly, reducing the overall precision for bright stars. Fainter stars would generally benefit from longer integration times, which at short t_{v}, can only be realized by reducing E. If the optical distortion correction is stable and a reference catalog can be constructed from all exposures of successive visits, while solving for the apparent motion of the stars between visits, one could reduce the number of per-visit exposures, resulting in increased precision for faint stars. In summary, the results in Figure 4 may be optimistic for bright stars and pessimistic for fainter ones.

5.2. Exoplanet Detectability

Given that we can achieve astrometric precisions of 10 μas or better with sufficiently long visit times, detecting exoplanets around nearby stars becomes feasible (e.g., Perryman et al. 2014; Sozzetti 2015 for studies on *Gaia*'s capabilities). We now seek to determine the general characteristics of exoplanet systems detectable with diffraction-spike measurements.

The astrometric signature of an exoplanet of mass M_{p}, orbiting a star of mass $M_* \gg M_{\mathrm{p}}$ with a semimajor axis a at a distance of d from the observer is given by

$$\left(\frac{\alpha}{1\ \mathrm{as}}\right) = \frac{M_{\mathrm{p}}}{M_*}\left(\frac{a}{1\ \mathrm{au}}\right)\left(\frac{d}{1\ \mathrm{pc}}\right)^{-1}. \tag{14}$$

With Kepler's third law,

$$p^2 = \frac{4\pi^2}{G\,M_*}a^3, \tag{15}$$

we can relate a to the orbital period p and re-express the astrometric signature in convenient units:

$$\left(\frac{\alpha}{1\ \mathrm{as}}\right) = \frac{M_{\mathrm{p}}}{M_\odot}\left(\frac{p}{1\ \mathrm{year}}\right)^{\frac{2}{3}}\left(\frac{M_*}{M_\odot}\right)^{-\frac{2}{3}}\left(\frac{d}{1\ \mathrm{pc}}\right)^{-1}. \tag{16}$$

For reference, the astrometric signature of the Earth–Sun system at a distance of 1 pc is $\approx$3 μas. With the measurement precision attainable here, exoplanet detection prefers planets that are either more massive or are on longer period orbits than Earth or stars less massive than the Sun.

The Extended Hipparcos Compilation (Anderson & Francis 2012, XHIP) lists 141 stars within 10 pc with magnitudes of $V_{\mathrm{Hip}} < 11$, which is approximately the range of stars useful for such a program. We take magnitudes R_J and J_{Vega} from XHIP and transform them to the AB system according to Frei & Gunn (1994) and Blanton et al. (2005).[7] We estimate their mass from the spectral type and show their distance–mass distribution in Figure 5. We also show the range of stellar masses and distances that would correspond to an astrometric signature of {3, 5, 10} μas for a hypothetical planet with $M_{\mathrm{p}} = 3M_\oplus$ and a period of 1 year.

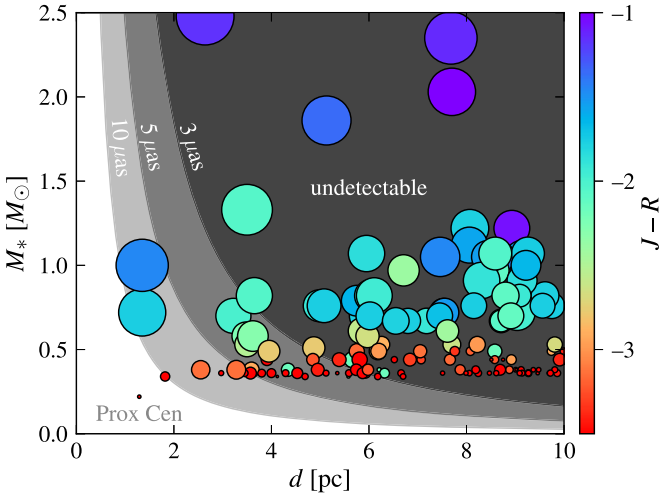

Figure 5. Stars from the Extended Hipparcos Compilation within $d = 10$ pc and $V_{\mathrm{Hip}} < 11$. Masses are calculated from the spectral type. Colors indicate $J - R$ and size the apparent brightness in V_{Hip}. The shaded regions correspond to detections given astrometric signatures of {3, 5, 10} μas for a hypothetical planet with $M_{\mathrm{p}} = 3M_\oplus$ and a period of 1 year (lighter is easier to detect).

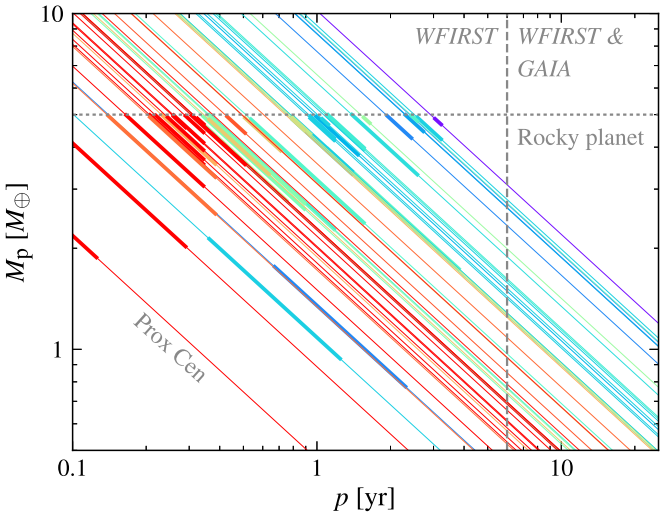

Figure 6. Minimal detectable mass of hypothetical planets around the most promising target stars from Figure 5, assuming an astrometric precision of 3 μas. The color scheme is identical to that in Figure 5. Thick parts of the lines indicate the habitable zone of the star for a rocky planet (applicable for $M\mathrm{p} < 5M_\oplus$, see the text for details).

The minimal detectable planet mass for the best target stars are shown in Figure 6; the 10 stars with the best astrometric precisions are listed in Table 2. We assume that the stars host a single-planet system and have a detection threshold of $\Delta_{\mathrm{pos,v}} = 3\ \mu$as.[8] While we adopt the most powerful prediction of the per-visit astrometry for this figure, this is still somewhat

[7] For stars on our list, XHIP does not list R_J or J_{Vega}. We then estimate the magnitudes from V_{Hip} and the spectral type.

[8] This detection criterion is obviously simplistic. In detail, the ability to detect an exoplanet sensitively depends on the orbital parameters, the number and configuration of planets in the system, as well as several observational parameters besides the per-visit astrometric precision, including cadence and total duration of the program (Casertano et al. 2008; Perryman et al. 2014). A thorough investigation of *WFIRST*'s exoplanet detection is thus beyond the scope of this work.

Table 2
Target Starts with the Highest Astrometric Precision from the Extended Hipparcos Compilation within $d = 10$ pc and $V_{\rm Hip} < 11$ (cf. Figure 5)

Name	Type	d (pc)	$V_{\rm Hip}$	η ($M_\oplus$)
α Cen C	M6	1.29	10.76	0.47
Gliese 699	M4	1.82	9.49	0.89
α Cen B	K1	1.35	1.24	1.08
Gliese 411	M2	2.55	7.51	1.34
α Cen A	G2	1.35	0.14	1.35
Gliese 729	M3	2.97	10.41	1.50
Gliese 887	M2	3.28	7.42	1.72
Gliese 725 B	M3	3.45	10.00	1.75
Gliese 725 A	M3	3.57	8.92	1.81
Gliese 15 A	M2	3.59	8.15	1.88

Note. We list spectral type, distance, and $V_{\rm Hip}$ directly from XHIP, ordered by an astrometric sensitivity η, which we define as the minimum mass of a single planet on a circular orbit with a period of 1 year assuming an astrometric precision of 3 μas.

conservative because detection should be possible with several visits even if the planet has a smaller α. Earth-mass planets become detectable around several of the nearby stars, albeit with orbits often longer than 1 year. As expected, dwarf stars provide the best targets, irrespective of their distance. It is therefore not surprising that Proxima Centauri (α Cen C) is by far the best individual target given its low mass and distance of only 1.29 pc, followed by Gliese 699, and the two other, more massive stars of the α Cen system.

We also investigate whether the hypothetical planets would occupy the habitable zones (HZ) of their stars. Using the optimistic limits ("recent Venus" to "early Mars" from Kopparapu et al. 2013) for planets with rocky composition ($M\,{\rm p} < 5M_\oplus$, Seager 2010), which depend only on stellar flux and temperature, we determine the corresponding periods p and show them with thick lines in Figure 6. Stars with effective temperatures below 2600 K or above 7200 K are excluded, and we ignore any dependence on the planet mass, which mostly affects the inner edge of the HZ (Kopparapu et al. 2014). Unfortunately, low-mass stars, nominally best for astrometric measurements, have HZs with small p, a regime that is hard to access astrometrically. Nonetheless, with an astrometric precision of 3 μas, we would be able to find planets with rocky compositions at the outer edges of their HZs. In addition, the G- and K-type stars α Cen A and α Cen B are the only stars for which Earth-mass planets could be found with Earth-like periods.

Several more stars from our list (not shown in Figure 6 for the sake of clarity) would add to the discovery potential of Neptune-class planets, especially on long orbits. Realistically, long orbital periods are limited by the lifetime of *WFIRST*, currently specified as 6 years (Spergel et al. 2015). A substantial extension to $\approx$16 years is possible if we add measurements from *Gaia*.

5.3. Synergies with other Instruments

WFIRST's coronagraphic instrument (CGI) should be the most sensitive coronagraph for the foreseeable future, with the ability to achieve contrast ratios of 10^9, a thousand-fold increase over *JWST* and *HST*. With an inner working angle of $\sim$0.1 as, it will be targeting many exoplanet systems that are also favorable astrometric targets: planets around bright stars with periods of $\sim$1–10 years. These targets will range from super-Earths to Jupiters. There are several potential synergies between *WFIRST* astrometric and coronagraphic observations. The astrometric program could discover planets that are potential targets for coronagraphic observations. Most exciting, by observing the same planet with the coronagraph and a program of astrometric observations, we will have measurements of the planet's mass and the composition of its atmosphere.

WFIRST is also being built to be ready for a "starshade" occulter. The combination of a starshade and *WFIRST* will enable higher throughputs and contrast ratios than a coronagraph (Roberge et al. 2015). Just as with the CGI, the astrometric measurements are a powerful complement to the exoplanet imaging. The astrometry can make the imaging observations more efficient and can increase the confidence of a detection. Again, the combination of a mass measurement and atmospheric characterization will yield deeper insights into exoplanet properties.

Table 3 lists some of the anticipated targets of the *WFIRST* CGI and starshade (J. Kasdin & B. Nemati 2017, private communication). In the last column, we list the astrometric sensitivity η (with the same definition as in Table 2) to illustrate minimal detectable planet masses. Given that the listed starshade targets are more nearby, astrometric measurements will be more sensitive overall; however, there is a large overlap with Neptune-like planets that CGI is expected to target. For stars with larger distances, astrometric targets would be restricted to Jupiter-like planets, again in good complementarity to the coronagraph.

6. Conclusion

We constructed an analytical model of the *WFIRST* diffraction spikes generated by a single support strut obscuring the telescope aperture. This model is a very reasonable description of the actual PSF outside of the first diffraction minimum. By propagating Poisson noise from the star, the sky, and the thermal emission of the telescope, as well as read-out noise and dark current, we determine that centering on the diffraction spikes of *WFIRST* allows for an astrometric precision of 10 μas for a $R = 6$ of $J = 5$ star in a 100 s exposure. The best attainable precision at a fixed magnitude is realized in the bluest filters because the diffraction spikes are the narrowest.

Given that both the diffraction spike measurement and the systematic contributions from optical distortions and pixel-level artifacts yield diminishing returns for longer integrations, more precise astrometry can be achieved with a series of exposures with $t \lesssim 100$ s. To better determine the optical distortion pattern and to account for possible spatial correlations of pixel-level artifacts, these exposures should be offset by about 100 pixels or more, which is the range in which most of the information about the stellar center is contained. We find that with an assumed systematic uncertainty of 20 μas per exposure, a per-visit precision of better than 10 μas can be achieved for $R < 7.5$ or $J < 6.5$ stars with total visit times of 1000 s or less.

For such bright stars, the measurement is limited by systematics. Uncorrected optical distortions or small-scale flaws, e.g., from subpixel QE variations or persistence, can quickly dominate the overall precision of the measurement. It will be critical for reproducible precision astrometry that the

Table 3
Prospective Targets for the *WFIRST* CGI and Starshade

Name	CGI	Starshade	Type	d (pc)	V	η ($M_\oplus$)
α Cen A		✓	G2	1.35	0.14	1.35
α Cen B		✓	K1	1.35	1.24	1.08
α CMa A		✓	A1	2.64	−1.47	4.21
ϵ Eri	✓	✓	K2	3.22	3.87	2.54
61 Cyg		✓	K5	3.48	5.37	2.42
α CMi A		✓	F5 IV-V	3.51	0.34	4.60
ϵ Ind		✓	K5	3.62	4.83	2.52
τ Cet		✓	G8.5	3.65	3.50	3.10
Gliese 832	✓		M2	4.95	8.70	2.60
40 Eri A		✓	K0	4.98	4.43	4.43
70 Oph A		✓	K0	5.08	6.00	4.75
α Aqu		✓	A7	5.13	0.76	7.56
σ Dra		✓	G9	5.76	4.67	5.17
η Cas A		✓	G0	5.95	3.44	5.83
36 Oph A		✓	K2	5.98	5.08	5.36
82 Eri		✓	G8	6.04	4.25	4.72
δ Pav		✓	G8 IV	6.11	3.56	6.07
β Hyi		✓	G2 IV	7.46	2.80	7.85
π^3 Ori		✓	G2 IV	8.07	3.16	9.29
β Gem	✓		K0 III	10.3	1.14	16.6
55 Cnc A	✓		G8	12.3	5.95	11.8
υ And	✓		F8	13.5	4.09	15.9
47 UMa	✓		G1	14.1	5.03	14.8
μ Ara	✓		G3	15.5	5.12	16.5
Gliese 777	✓		G6 IV	15.9	5.71	14.8
14 Her	✓		K0	17.6	6.67	16.4
HD 87883	✓		K0	18.2	7.56	15.9
HD 39091	✓		G1 IV	18.3	5.67	19.6
HD 154345	✓		G8	18.6	6.74	17.1
HD 217107	✓		G8 IV	19.9	6.17	19.4
HD 114613	✓		G4 IV	20.7	4.85	24.0
ψ Dra B	✓		F8	23.1	5.82	25.9
HD 142	✓		F7	25.7	5.71	29.8
HD 134987	✓		G5	26.2	6.45	27.0

Note. We list spectral type, distance, V magnitude, and astrometric sensitivity η, which we define as the minimum mass of a single planet on a circular orbit with a period of 1 year assuming an astrometric precision of 3 μas.

optical distortion model is well constrained at least in the central regions of the detectors. We believe that these challenges can be met given *WFIRST*'s thermally stable environment in the L2 orbit and the calibration products from the microlensing program and dedicated calibration campaigns in high-stellar density fields.

An astrometric exoplanet discovery program with *WFIRST* could detect Earth-mass planets with orbital periods of 1 year or more as well as Neptune-like planets with shorter periods around bright starts within ∼10 pc. Combining with the measurements from *Gaia* could additionally provide access to the regime of rocky planets with periods of 10 years or longer. An astrometric observing program would complement the *WFIRST* direct-imaging program and provide masses and orbits for planets whose atmospheres are characterized with either a starshade or coronagraph.

P.M. thanks Andrea Bellini, Stefano Casertano, Craig Loomis, and Jim Gunn for instructive discussions. This research has been supported by the NASA *WFIRST* program. The Flatiron Institute is supported by the Simons Foundation.

Software: WebbPSF (Perrin et al. 2012, 2014).

Appendix
Pixel-integrated PSF of a Rectangular Obstruction, and Its Derivatives

Realizing that both the PSF intensity in Equation (2) as well as the pixel shape in Equation (3) are separable into two one-dimensional (1D) functions, we can break down the entire integral into 1D. We utilize the convolution theorem and the following known analytic results for Fourier transforms:

$$\mathrm{FT}[f(x)](q) \equiv \frac{1}{\sqrt{2\pi}} \int dx\, f(x) e^{-iqx} \tag{17}$$

$$\mathrm{FT}[\mathrm{rect}(cx)](q) = \frac{1}{\sqrt{2\pi c^2}}\, \mathrm{sinc}\left(\frac{q}{2c}\right) \tag{18}$$

$$\mathrm{FT}[\mathrm{sinc}^2(cx)](q) = \frac{2}{\sqrt{2\pi c^2}}\, \mathrm{tri}\left(\frac{q}{2c}\right), \tag{19}$$

where $\mathrm{tri}(x) \equiv \mathrm{rect}(x/2)(1 - |x|)$. We can now express the x-part of Equation (3) as follows:

$$\mathrm{FT}[I_p(x)] = \frac{2}{\sqrt{2\pi}\, k_x}\, \mathrm{tri}\left(\frac{q}{2k_x}\right) \frac{w}{\sqrt{2\pi}}\, \mathrm{sinc}\left(\frac{qw}{2}\right). \tag{20}$$

The inverse Fourier transform of that equation is

$$\begin{aligned} I_p(x \mid k, w) = {} & \frac{1}{k\pi(w^2 - 4x^2)}[[-2w + 2w\cos(kw) \\ & \times \cos(2kx) + 4x\sin(kw)\sin(2kx) + k(w^2 - 4x^2) \\ & \times [\mathrm{Si}(k(w - 2x)) + \mathrm{Si}(k(w + 2x))]], \end{aligned} \tag{21}$$

where Si denotes the sine integral, and we already applied a normalization of $\sqrt{\frac{2}{\pi}}\frac{w}{k}$ so that the function integrates to unity.

The derivatives of this function are

$$\begin{aligned} & \frac{\partial I_p(x \mid k, w)}{\partial x} \\ & = \frac{16wx(-1 + \cos(kw)\cos(2kx)) + 4(w^2 + 4x^2)\sin(kw)\sin(2kx)}{k\pi(w^2 - 4x^2)^2} \end{aligned} \tag{22}$$

$$\begin{aligned} \frac{\partial^2 I_p(x \mid k, w)}{\partial x^2} = {} & \frac{8}{k\pi(w^2 - 4x^2)^3}[-2w(w^2 + 12x^2) \\ & + \cos(2kx)(2w(w^2 + 12x^2)\cos(kw) \\ & + k(w^4 - 16x^4)\sin(kw)) \\ & + 4x(-kw(w^2 - 4x^2)\cos(kw) \\ & + (3w^2 + 4x^2)\sin(kw))\sin(2kx)]. \end{aligned} \tag{23}$$

ORCID iDs

Peter Melchior https://orcid.org/0000-0002-8873-5065

References

Anderson, E., & Francis, C. 2012, AstL, 38, 331
Anderson, J., & King, I. R. 2003, PASP, 115, 113
Barron, N., Borysow, M., Beyerlein, K., et al. 2007, PASP, 119, 466
Bellini, A., Anderson, J., & Bedin, L. R. 2011, PASP, 123, 622
Blanton, M. R., Schlegel, D. J., Strauss, M. A., et al. 2005, AJ, 129, 2562
Casertano, S., Lattanzi, M. G., Sozzetti, A., et al. 2008, A&A, 482, 699

Frei, Z., & Gunn, J. E. 1994, AJ, 108, 1476
Gaia Collaboration, Prusti, T., de Bruijne, J. H. J., et al. 2016, A&A, 595, A1
Gould, A., Huber, D., Penny, M., & Stello, D. 2015, JKAS, 48, 93
Hardy, T., Willot, C., & Pazder, J. 2014, Proc. SPIE, 9154, 91542D
Kopparapu, R. K., Ramirez, R., Kasting, J. F., et al. 2013, ApJ, 765, 131
Kopparapu, R. K., Ramirez, R. M., SchottelKotte, J., et al. 2014, ApJL, 787, L29
Libralato, M., Bellini, A., Bedin, L. R., et al. 2014, A&A, 563, A80
Perrin, M. D., Sivaramakrishnan, A., Lajoie, C.-P., et al. 2014, Proc. SPIE, 9143, 91433X
Perrin, M. D., Soummer, R., Elliott, E. M., Lallo, M. D., & Sivaramakrishnan, A. 2012, Proc. SPIE, 8442, 84423D
Perryman, M., Hartman, J., Bakos, G. Á., & Lindegren, L. 2014, ApJ, 797, 14
Plazas, A. A., Shapiro, C., Smith, R., Rhodes, J., & Huff, E. 2017, arXiv:1703.08205
Riess, A. G., Casertano, S., Anderson, J., MacKenty, J., & Filippenko, A. V. 2014, ApJ, 785, 161
Roberge, A., Seager, S., Thomson, M., et al. 2015, in Pathways Towards Habitable Planets, 92
Seager, S. (ed.) 2010, in Exoplanets (Tucson, AZ: Univ. Arizona Press), 526
Sozzetti, A. 2015, arXiv:1502.03575
Spergel, D., Gehrels, N., Baltay, C., et al. 2015, arXiv:1503.03757
Spergel, D., Gehrels, N., Breckinridge, J., et al. 2013, arXiv:1305.5422
The WFIRST Astrometry Working Group, Sanderson, R. E., Bellini, A., et al. 2017, arXiv:1712.05420